nature research

https://doi.org/10.1038/s41565-020-0758-6

Supplementary information

Photonic Rashba effect from quantum emitters mediated by a Berry-phase defective photonic crystal

In the format provided by the authors and unedited

nature research

https://doi.org/10.1038/s41565-020-0758-6

Supplementary information

Photonic Rashba effect from quantum emitters mediated by a Berry-phase defective photonic crystal

In the format provided by the authors and unedited

Photonic Rashba effect from quantum emitters mediated by a Berry-phase defective photonic crystal

Kexiu Rong[1,3], Bo Wang[1,3], Avi Reuven[1], Elhanan Maguid[1], Bar Cohn[1], Vladimir Kleiner[1], Shaul Katznelson[2], Elad Koren[2] and Erez Hasman[1*]

Supplementary Information for

Photonic Rashba effect from quantum emitters mediated by a Berry-phase defective photonic crystal

Kexiu Rong[1,3], Bo Wang[1,3], Avi Reuven[1], Elhanan Maguid[1], Bar Cohn[1], Vladimir Kleiner[1], Shaul Katznelson[2], Elad Koren[2] and Erez Hasman[1*]

This supplementary information consists of 11 sections in support of the main body of the text. The contents of the sections are listed below:

Section 1: Fabrication of sample

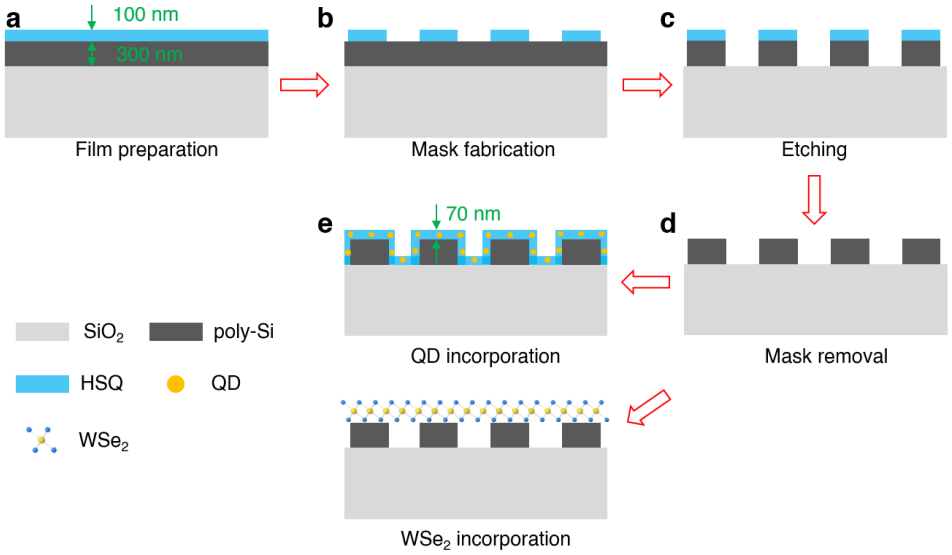

Supplementary Fig. 1 | Fabrication processes of the sample. a, Preparation of the poly-Si and HSQ films above the SiO_2 substrate. **b**, Fabrication of the HSQ mask. **c**, Etching of the uncovered poly-Si film. **d**, Removal of the HSQ mask. **e**, Incorporation of the QDs or WSe_2 monolayer. Detailed descriptions can be found in Fabrication Section of Methods in the main text.

Section 2: Experimental setup

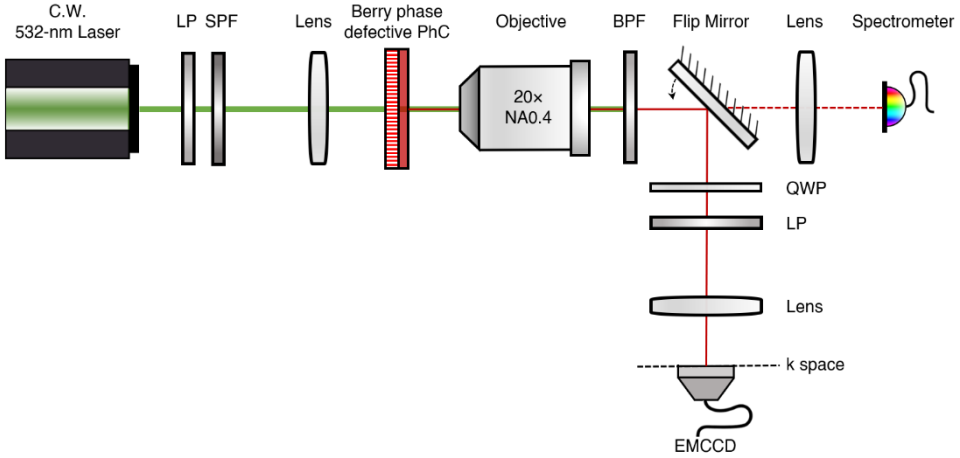

Supplementary Fig. 2 | Schematic of the experimental setup. LP, linear polarizer; SPF, short-pass filter; BPF, bandpass filter; QWP, quarter-wave plate; EMCCD, electron multiplying charge-coupled device. The cut-off wavelength for the short-pass filter is 650 nm. The focal lengths for all lenses are f = 10 cm. In the measurements, five different bandpass filters with central wavelengths of 700 nm, 720 nm, 740 nm, 760 nm, and 790 nm are employed, and the half-maximum bandwidths for them are 10 nm. Detailed descriptions can be found in Measurement Section of Methods in the main text.

Section 3: Principle of Berry-phase defective PhC

Defect band

As demonstrated in the main text, the defect band for the Berry-phase defective PhC (green dots in Supplementary Fig. 3a) is attributed to a hopping mechanism between neighboring defects, whereby the Berry phase defect mode with space-variant local field distributions is formed (see Supplementary Fig. 3b for its field distribution in a complete unit cell). For comparison, we also calculated the defect band for a defective PhC with all the defects possessing the same orientation $\theta(x,y) = 0$, as shown by the orange dots in Supplementary Fig. 3a. It is noticed that the defect bands for these two cases are identical, which reveals that the hopping effect is determined by the subwavelength period of the defect lattice, irrespective of the specific orientations of the defects. The identical defect band for two orientation profiles also indicates that the defect band is robust against the orientation disorder in fabrication. Other disorders in fabrication, such as the small size variation, only contribute to a small wavelength shift of the wide defect band (wavelength range~20 nm), which has a negligible influence on the overlap between the defect band and the broadband PL (~100 nm).

The defect band for the Berry-phase defective PhC (Fig. 2b) is separately fitted by the dispersion relation $\omega \propto 1+\kappa\cos(KR)$ along M-X and M-Γ directions with coupling factors κ_1 = 0.019 and κ_2 = 0.013, respectively. Here, ω denotes the frequency and K denotes the wavenumber of the defect band in the first Brillouin zone. The stronger hopping effect along the M-X direction is attributed to a shorter distance between neighboring defects in this direction ($R_1 / R_2 \approx 1/\sqrt{2}$). The strength of the hopping effect can be controlled by changing the lattice constant of the square lattice: the smaller the defect lattice constant, the stronger the hopping effect, as revealed by the coupling factors under different lattice constants (Supplementary Fig. 3c). Here, the orange and blue dots correspond to coupling factors along M-X and M-Γ directions, respectively.

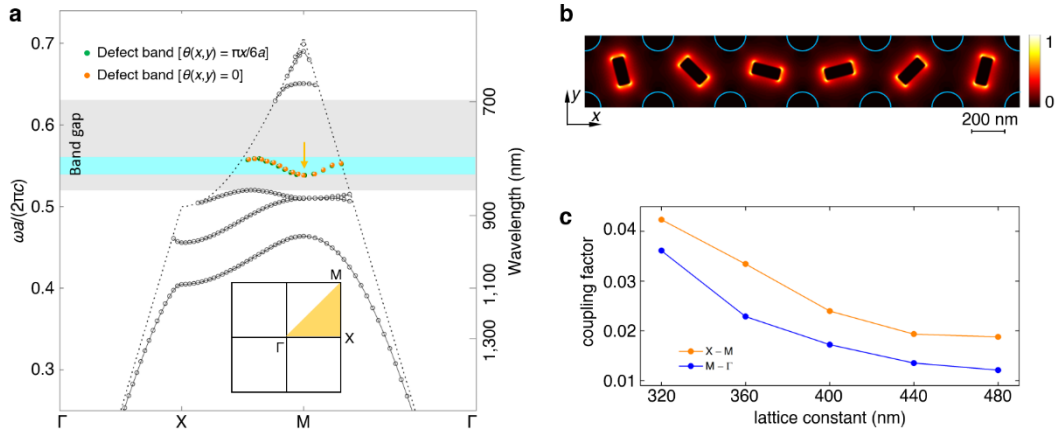

Supplementary Fig. 3 | Defect band originating from hopping effect. a, Calculated defect bands for Berry-phase defective PhC ($\theta(x,y) = \pi x/6a$, orange dots) and reference defective PhC ($\theta(x,y) = 0$, green dots). Except for the defect band for the reference structure, other contents are the same as Fig. 2a. **b**, Intensity distribution of the in-plane electric field at M point of the defect band in a complete unit cell. **c**, Fitted coupling factors under different lattice constants. The orange and blue dots correspond to coupling factors along M-X and M-Γ directions, respectively.

Propagation of photons via hopping

To demonstrate the propagation of photons through neighboring defects via hopping, we simulated a finite square PhC slab (12 × 12 unit cells) embedded with six space-variant nanoantennas, wherein a single *x*-oriented dipole is utilized to excite the structure at one of the defects (Supplementary Fig. 4a). The emerging field distribution at the wavelength of the defect mode demonstrates the hopping effect; that is, defect modes supported by defects away from the source are also excited via coupling between neighboring defects, which gives rise to the Berry phase defect mode. As a reference, no hopping effect and Berry phase defect mode are observed in the absence of the PhC slab, as shown in Supplementary Fig. 4b.

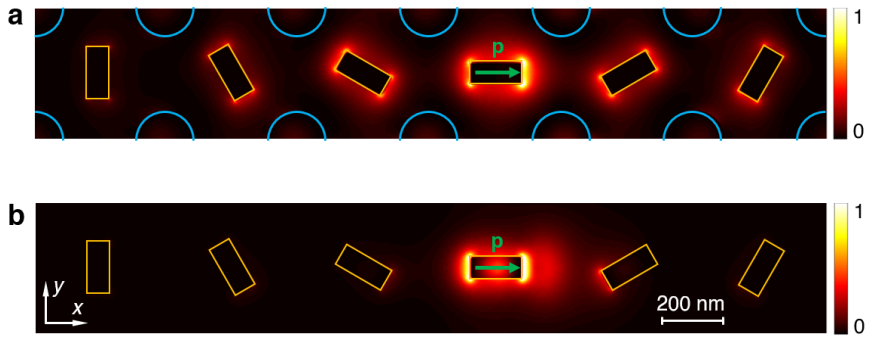

Supplementary Fig. 4 | Hopping effect and Berry phase defect mode. a, Intensity distribution of the in-plane electric field for a finite square PhC slab embedded with space-variant nanoantennas as defects. **b**, Similar to **a** without the PhC slab. The dipole emitters are indicated by the green arrows. These distributions are obtained at the wavelength of the defect mode.

PL enhancement factor

Here, we calculated the enhancement of emission from WSe_2 monolayer that is incorporated in the Berry-phase defective PhC. The PL enhancement factor $\langle EF \rangle$[1] is defined as the product of the excitation efficiency η and the Purcell factor F_P at the monolayer plane, which is assumed to be 1 nm above the top surface of the nanostructures. Specifically, the excitation efficiency is determined by the field enhancement of the pump beam as $\eta = |E_{\parallel}/E_0|^2$, in which E_0 and $E_{\parallel}$ are the electric field

amplitudes for the incident pump beam and the resultant in-plane near field of the nanostructures, respectively. Here, only the in-plane electric field components are considered because the PL in the WSe_2 monolayer originates from in-plane valley excitons. In the calculation, an *x*-polarized plane wave ($\lambda_p = 533$ nm) normally impinges onto the Berry-phase defective PhC, and the obtained excitation efficiency in one of the unit cells is depicted in Supplementary Fig. 5a. The excitation efficiency is enhanced by an order of magnitude around the defect, in favor of the site-controlled excitation of the quantum emitters.

On the other hand, the Purcell factor describes the decay rate enhancement of spontaneous emission from an emitter, ascribed to the modification of its local density of states by nanostructures. According to the correspondence between the quantum and classical analyses of spontaneous emission[2], the decay rate enhancement equals the enhancement of the radiated power of the emitter, namely, $F_P = P/P_0$; here, P and P_0 denote the radiated power of the emitter incorporated in our Berry-phase defective PhC and in vacuum, respectively. In the calculation, we scan the location of a single electric dipole (at the wavelength of defect mode, $\lambda_e = 800$ nm) in a unit cell at the monolayer plane, and record its radiated power P at each position, which is normalized by P_0 for calculating the Purcell factor. The dipole of both *x*- and *y*-orientations are implemented, which give the *x*- and *y*-polarized Purcell factors (F_{Px} and F_{Py}), respectively. Since the valley excitons radiate as in-plane circular dipoles, we define the Purcell factor for the valley excitons as $F_P = \sqrt{F_{Px}^2 + F_{Py}^2}$, and the calculated results are depicted in Supplementary Fig. 5b. Due to the tailored local density of states by the Berry phase defect mode, the emission enhancement is mainly achieved around the defect by twenty times.

The calculated PL enhancement factor ($<EF> = \eta \times F_P$) for the WSe_2 monolayer is displayed in Supplementary Fig. 5c. The strong PL enhancement around the defect leads to a tailored light-matter interaction between site-controlled emitters and the Berry phase defect mode. Hence, the measured spin-dependent directional emission in momentum space is dominated by emitters close to the defects, validating the assumption of dipole emitters at the defect positions in equation (1). Other emitters away from the defects mainly radiate to the background field or spin-independent directional emission in momentum space. By integrating the PL enhancement factor around the nanopillars, we estimate that these emitters only account for 20% of the total PL intensity.

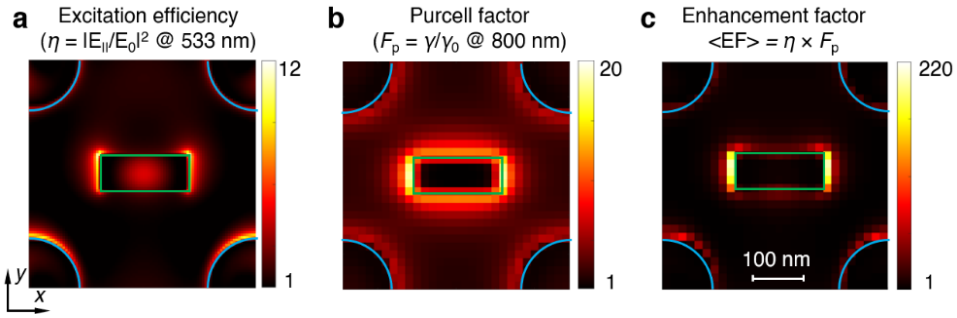

Supplementary Fig. 5 | Calculated excitation efficiency, Purcell factor, and PL enhancement factor for emitters incorporated in Berry-phase defective PhC. These results are obtained at 1 nm above the top surface of the nanostructures. Only one unit cell of the structure is shown here since similar results can be observed for other unit cells. The contours of the defect and nanopillar are highlighted by the green rectangle and cyan quarter circle, respectively.

Section 4: Raman spectra of WSe_2 monolayer

The highly-crystalline WSe_2 monolayer (1 cm × 1 cm), grown by chemical vapor deposition, was purchased from 2D Semiconductors. The as-grown WSe_2 monolayer uniformly covered a *c*-cut sapphire substrate, and the measured single Raman peak around 250 cm^{-1} confirms the monolayer character (black curve in Supplementary Fig. 6). Subsequently, the monolayer was transferred above the Berry-phase defective PhC on the fused silica substrate. After the transfer, the monolayer character remains, as confirmed by the stable single Raman peaks (red and blue curves in Supplementary Fig. 6).

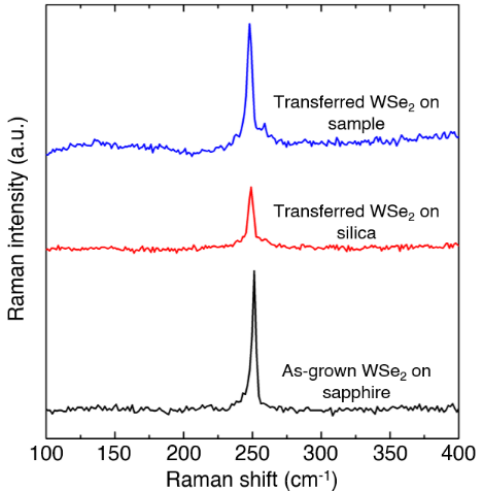

Supplementary Fig. 6 | Measured Raman spectra of WSe_2 monolayer. The as-grown WSe_2 on the sapphire substrate, transferred WSe_2 on the fused silica substrate, and transferred WSe_2 on the Berry-phase defective PhC are measured.

Section 5: Photonic Rashba effect from valley excitons

The PL scattered from the Berry-phase defective PhC was filtered out by different bandpass filters (Supplementary Fig. 7a) and spin-projected in momentum space. Supplementary Figs. 7b-d depict the measured PL intensity distributions for the Berry-phase defective PhC (Fig. 3c) covered with a WSe_2 monolayer under three different wavelengths: 740 nm, 760 nm, and 790 nm. The measurements for two opposite spin states ($I_{\sigma+}$ and $I_{\sigma-}$) are displayed by the left and right columns, respectively, where the spin-split modes are observed at λ = 760 nm and 790 nm. For wavelengths further away from 790 nm, such as λ = 740 nm, no spin-split mode can be observed. This is consistent with the measured wavelength range for PL enhancement in the Berry-phase defective PhC (Fig. 2c).

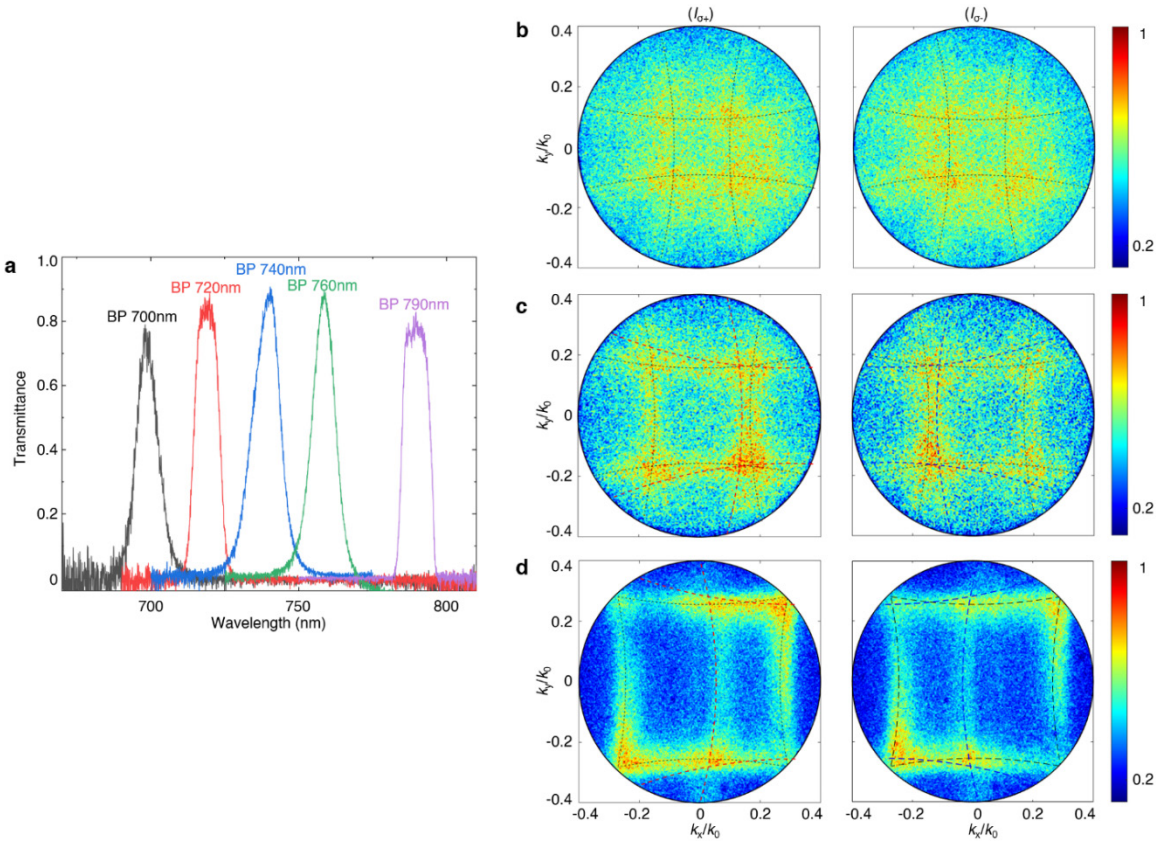

Supplementary Fig. 7 | Measured PL intensity distributions in momentum space for Berry-phase defective PhC covered with a WSe_2 monolayer. a, Measured transmission spectra for the bandpass filters. The central wavelengths of the BP filters are 700 nm, 720 nm, 740 nm, 760 nm, and 790 nm, and their half-maximum bandwidths are 10 nm. **b-d,** Measured PL intensity distributions in momentum space at central wavelengths of λ = 740 nm, 760 nm, and 790 nm, respectively. The left and right columns show the measured PL intensity distributions for the σ_+ and σ_- states, respectively. The dashed curves denote calculations based on the spin-orbit momentum-matching condition.

Section 6: Geometric phase from circular dipole

To model the interaction between a dipole emitter and the defect lattice (Supplementary Fig. 8a), the defects are assumed to behave as perfect polarizers with transmission axes $\hat{\mathbf{P}}_n = \cos\theta_n \hat{\mathbf{x}} + \sin\theta_n \hat{\mathbf{y}}$ following the orientations θ_n of the defects, as validated by the measured polarization locking along the defects (Fig. 3b). For a circular dipole of either left (+) or right (-) handedness with dipole moment $\mathbf{p}_m^{\pm} = p(\hat{\mathbf{x}} \pm i\hat{\mathbf{y}})$, the emerging phase for its spin-flipped component of radiation consists of two parts: geometric phase and dynamic phase; that is, $\arg\{[(\mathbf{E}_{\pm}^m(\mathbf{r}_n)\cdot\hat{\mathbf{P}}_n)\hat{\mathbf{P}}_n]\cdot\hat{\boldsymbol{\sigma}}^{\mp}\} = \phi_g(\mathbf{r}_n) + \phi_d(\mathbf{r}_n)$. Here, $\mathbf{E}_{\pm}^m(\mathbf{r}_n)$ is the radiated electric field from the left-handed or right-handed circular dipole at the *n-th* defect location $\mathbf{r}_n$; $\hat{\boldsymbol{\sigma}}^{\mp} = (\hat{\mathbf{x}} \mp i\hat{\mathbf{y}})/\sqrt{2}$ is a unit operator that projects the radiation to the spin-flipped state. The dynamic phase due to the phase accumulation from the source $\mathbf{p}_m$ to the *n-th* defect equals to the phase for the spin-maintained component of radiation, that is, $\phi_d(\mathbf{r}_n) = \arg\{[(\mathbf{E}_{\pm}^m(\mathbf{r}_n)\cdot\hat{\mathbf{P}}_n)\hat{\mathbf{P}}_n]\cdot\hat{\boldsymbol{\sigma}}^{\pm}\}$. Hence, the geometric phase from circular dipole is $\phi_g(\mathbf{r}_n) = \arg\{[(\mathbf{E}_{\pm}^m(\mathbf{r}_n)\cdot\hat{\mathbf{P}}_n)\hat{\mathbf{P}}_n]\cdot\hat{\boldsymbol{\sigma}}^{\mp}\} - \arg\{[(\mathbf{E}_{\pm}^m(\mathbf{r}_n)\cdot\hat{\mathbf{P}}_n)\hat{\mathbf{P}}_n]\cdot\hat{\boldsymbol{\sigma}}^{\pm}\}$. Based on this formula, we calculated the geometric phases from both left- and right-handed circular dipoles, and the results are in good agreement with the well-known relation $\phi_g(\mathbf{r}_n) = -2\sigma\theta_n{}^3$ (Supplementary Fig. 8b).

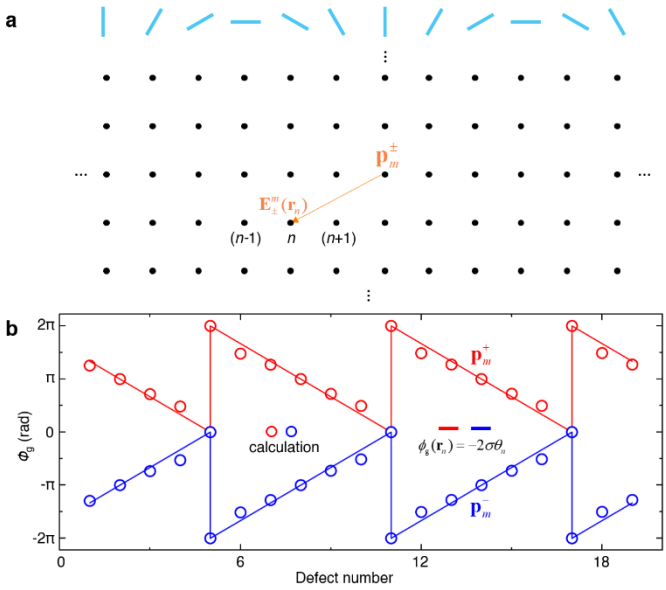

Supplementary Fig. 8 | Calculated geometric phase from circular dipole. a, Schematic of the model. The defects are treated as perfect polarizers following an orientation profile of $\theta(x,y) = \pi x/6a$, as indicated by the cyan bars. **b**, Calculated geometric phases from left- (red) and right-handed (blue) circular dipoles along a row of defects (λ = 790 nm). The circles denote the calculated values, while the lines denote the theoretical values of $\phi_g(\mathbf{r}_n) = -2\sigma\theta_n$.

Section 7: Spin-split spots from coherent dipole sources

Due to a lack of strong synchronizing mechanism, such as stimulated emission, quantum emitters incorporated in the Berry-phase defective PhCs radiated independently as multiple incoherent sources. Consequently, the continuous branches obeying the spin-orbit momentum-matching condition $\mathbf{k}_{\parallel}^{g,h} = n_{\text{eff}}\mathbf{k}_0 + g\mathbf{G}_1 + h\mathbf{G}_2 + \sigma\mathbf{k}_s$ were observed in momentum space (dashed red and blue curves in Supplementary Fig. 9). This situation changes when these sources become coherent, and the spin-resolved momentum space becomes $\overline{S}_3 = -2\,\mathrm{Im}(U_x U_y^*)/(|U_x|^2 + |U_y|^2)$, with $U_x = \sum_m U_x^m$ and $U_y = \sum_m U_y^m$; here, U_x^m and U_y^m are electric field components in momentum space for the *m-th* dipole source that is calculated by equation (1) in the main text. Supplementary Fig. 9 shows the calculated $\overline{S}_3$ from multiple coherent linear dipole emitters after interacting with the Berry-phase defective PhC. It is observed that the continuous branches collapse to discrete points, which result from the constructive interferences between these dipole sources. Note that two spin-split spots obeying $\mathbf{k}_{\parallel} = \sigma\mathbf{k}_s$ appear in this case, as indicated by the red and blue arrows in Supplementary Fig. 9.

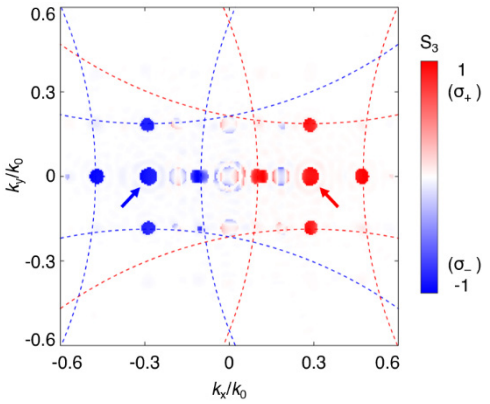

Supplementary Fig. 9 | Spin-split spots from coherent dipole sources. The structural parameters are the same as those in Fig. 3f. The dashed blue and red curves denote calculations based on the spin-orbit momentum-matching condition (λ = 760 nm).

Section 8: Photonic Rashba effect from QDs

For the Berry-phase defective PhC incorporated with QDs (Fig. 4a), we measured the spin-resolved PL intensity distributions in momentum space under five different wavelengths: 700 nm, 720 nm, 740 nm, 760 nm, and 790 nm. The measured PL intensity distributions for two opposite spin states ($I_{\sigma+}$ and $I_{\sigma-}$) are depicted by the left and middle columns in Supplementary Fig. 10,

respectively, while the right column shows the corresponding S_3 distributions. The scattered PL at each wavelength gives rise to a specific spin-split mode, and the extracted spin-split dispersion along $k_y = 0$ manifests as the photonic Rashba effect (Supplementary Fig. 11).

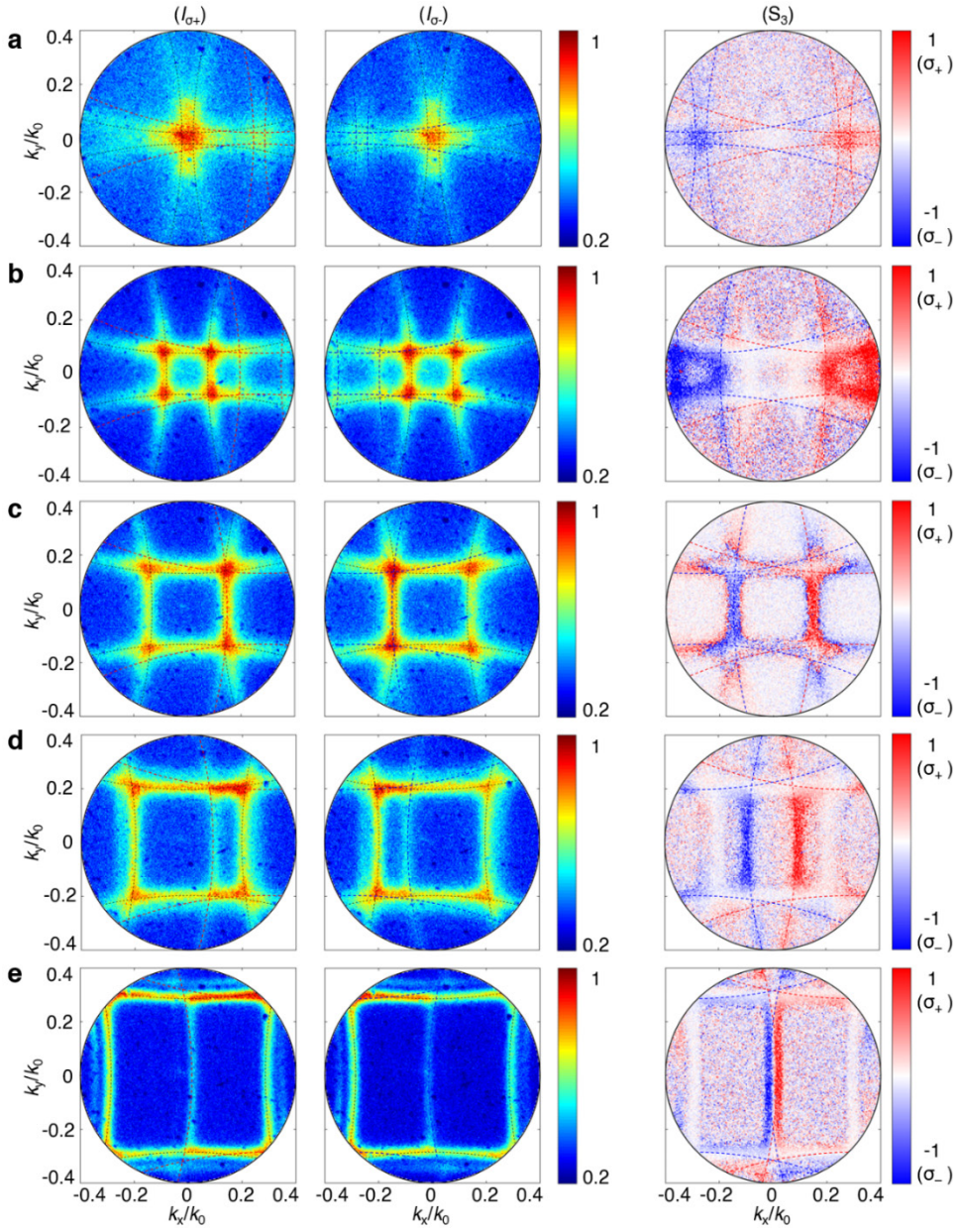

Supplementary Fig. 10 | Measured PL intensity and S_3 distributions in momentum space for Berry-phase defective PhC incorporated with QDs. a-e correspond to cases with central wavelengths of λ = 700 nm, 720 nm, 740 nm, 760 nm, and 790 nm, respectively. The left and middle columns show the measured PL intensity distributions for the σ_+ and σ_- states, respectively, while the right column shows the corresponding S_3 distributions. The dashed curves denote calculations based on the spin-orbit momentum-matching condition.

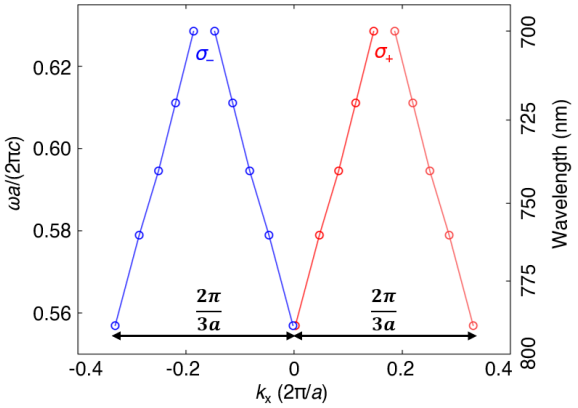

Supplementary Fig. 11 | Extracted spin-split dispersion along $k_y = 0$. Here, a is the lattice constant of the square PhC slab (a = 440 nm).

Section 9: Principle of Kagome-hexagonal Berry-phase defective PhC

Band gap and defect band

To calculate the band structure for the Kagome-hexagonal Berry-phase defective PhC, Bloch boundaries are employed in the x and y directions, and anti-symmetric boundaries are employed in the z direction. The unit cell of the simulation structure can be seen in Supplementary Fig. 12b. In the simulation, the heights of all the silicon nanostructures (refractive index of 3.4) are H = 300 nm. The in-plane dimensions of the rectangular nanoantennas are L = 170 nm and W = 70 nm, the diameters of the nanopillars are Φ = 90 nm. The refractive index of the surrounding environment is set to 1.3, which equals the effective refractive index (n_{eff}) used to fit the spin-split mode in Fig. 4e. Under this circumstance, the Kagome PhC slab also possesses a band gap (gray area in Supplementary Fig. 12a) covering the PL wavelengths of QDs (Fig. 4d). Besides, a defect band (green dots) emerges in the band gap when space-variant defects are embedded within the PhC slab. Note that a similar defect band (orange dots) is observed when defects with the same orientation are embedded in the PhC slab, which also implies that the defect band is attributed to the subwavelength period of the defect lattice.

Supplementary Fig. 12b depicts the calculated x-y field distribution at the Γ point of the defect band, where the Berry phase defect mode with space-variant local field distributions can also be observed. The experimental verification of the strong polarization manipulation in the Kagome-hexagonal Berry-phase defective PhC can be found in Supplementary Fig. 21a. In addition, the x-z field distribution reveals that the defect mode mainly resides around the defects for a good interaction with the quantum emitters, as shown in Supplementary Fig. 12c.

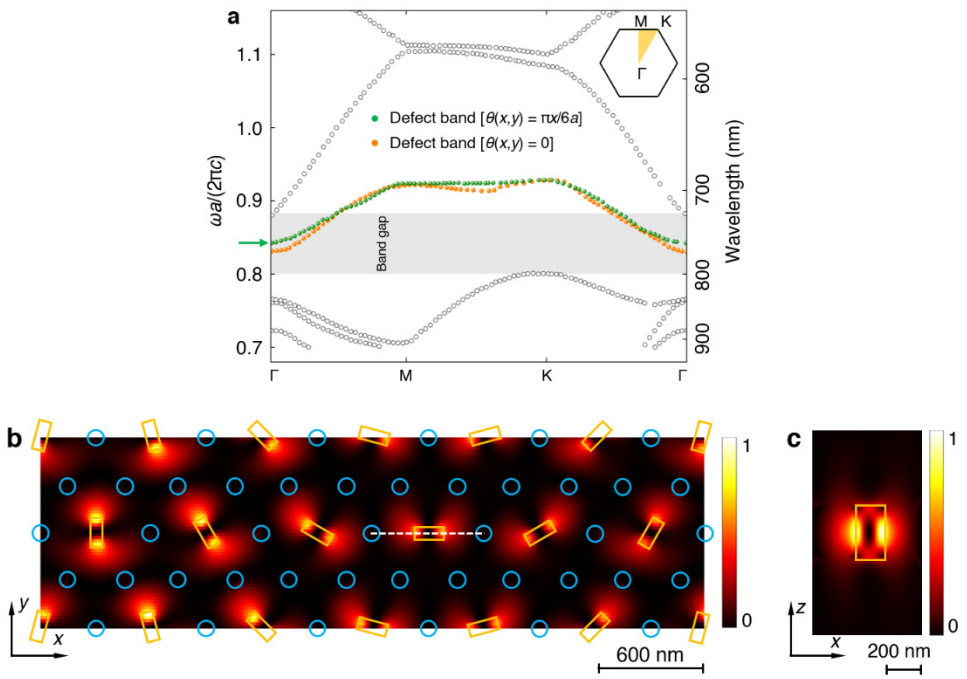

Supplementary Fig. 12 | Band gap and defect band. a, Calculated band structure for Kagome-hexagonal Berry-phase defective PhC. The green dots denote the defect band. For comparison, the defect band (orange dots) for the defective PhC with all the defects possessing the same orientation is also shown. The gray area indicates the band gap for the Kagome PhC slab. The inset shows the first Brillouin zone of the Kagome PhC slab labelled with high symmetry points. **b**,**c**, Electric-field-intensity distributions of the Berry phase defect mode on the *x*-*y* and *x*-*z* cross sections, respectively. The *x*-*y* cross section corresponds to the midplane of the nanostructures, while the position of the *x*-*z* cross section is marked by a dashed line in **b**. The simulation wavelength corresponds to the Γ point of the defect band, as indicated by a green arrow in **a**. The orange rectangles and cyan circles indicate contours of the nanoantennas and nanopillars, respectively.

Hopping effect and field enhancement

Similar to Supplementary Fig. 4, we also demonstrated the propagation of photons through neighboring defects via hopping in the Kagome-hexagonal Berry-phase defective PhC, whereby the Berry phase defect mode is formed (Supplementary Fig. 13a). Likewise, an *x*-oriented dipole (green arrow) is employed to excite the finite Kagome PhC slab (15 × 11 unit cells) embedded with six space-variant nanoantennas. In contrast, no hopping effect and Berry phase defect mode are observed in the absence of the PhC slab. Moreover, we calculated the field distributions for the PhC slab and an isolated nanoantenna under the same excitation condition (Supplementary Fig. 14a). It is revealed that the weak resonance of the isolated nanoantenna is enhanced by more than an order of magnitude when embedded within the PhC slab (Supplementary Fig. 14b). This will also lead to site-controlled quantum emitters around the defects by the Purcell effect. The measured

PL enhancement for the Kagome-hexagonal Berry-phase defective PhC (compared to the case of a bare QD-doped HSQ film) is depicted in Fig. 4d, where a fivefold enhancement is achieved.

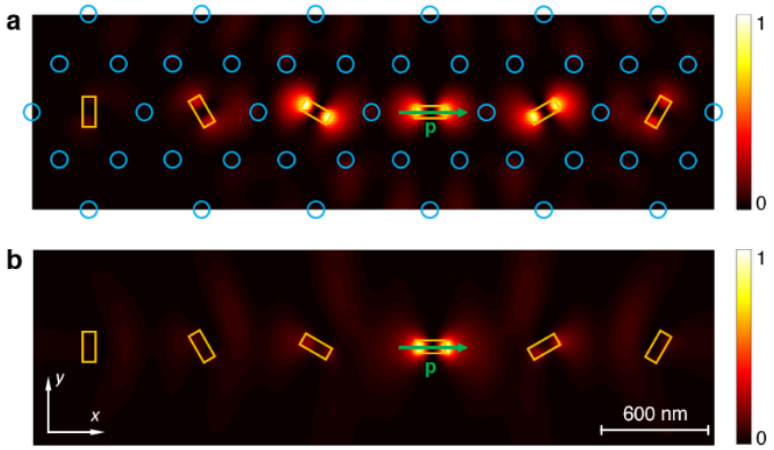

Supplementary Fig. 13 | Hopping effect and Berry phase defect mode. a, Electric-field-intensity distribution for a finite Kagome PhC slab embedded with space-variant nanoantennas as defects. **b**, Similar to **a** without the PhC slab. The dipole emitters are indicated by the green arrows. These distributions are extracted across the midplane of the nanostructures at the wavelength of the defect mode.

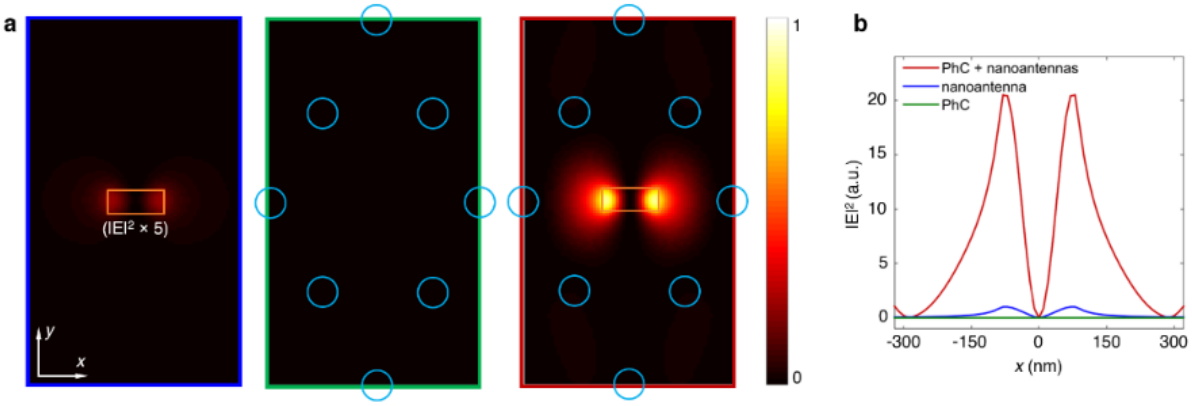

Supplementary Fig. 14 | Intensity enhancement of nanoantenna resonance via Kagome PhC slab. a, Electric-field-intensity distributions for the isolated nanoantenna, PhC slab, and defective PhC with space-variant defects (one defect along $\theta = 0$ is shown), respectively. These distributions are extracted across the midplane of the nanostructures at the wavelength of the defect mode. Only one unit cell of the PhC slab is displayed for the last two cases. **b**, Extracted electric-field-intensity profiles along the x direction. These profiles are extracted across the center of the nanoantenna from the x-y distributions shown in **a**. The intensity profile of the isolated nanoantenna is used for normalization.

Section 10: Photonic Rashba effect from QDs incorporated in Kagome-hexagonal Berry-phase defective PhC

The spin-projected measurements were also conducted for the Kagome-hexagonal Berry-phase defective PhC incorporated with QDs (Fig. 4c). The measured wavelength-dependent spin-split modes for five different wavelengths are displayed in Supplementary Fig. 15. The photonic Rashba effect can also be observed in this lattice configuration, as demonstrated by the extracted spin-split dispersion along $k_y = 0$ in the main text (Fig. 4f). Furthermore, the calculated spin-split efficiency, defined as the intensity ratio $(I_+ + I_-)/(I_{GM} + I_+ + I_-)$, is approximately 50%. Here, I_+, I_-, and I_{GM} are intensities for spin-up mode, spin-down mode, and the corresponding grating mode determined by the standard momentum-matching condition, respectively; these intensity values are obtained along $k_y = 0$.

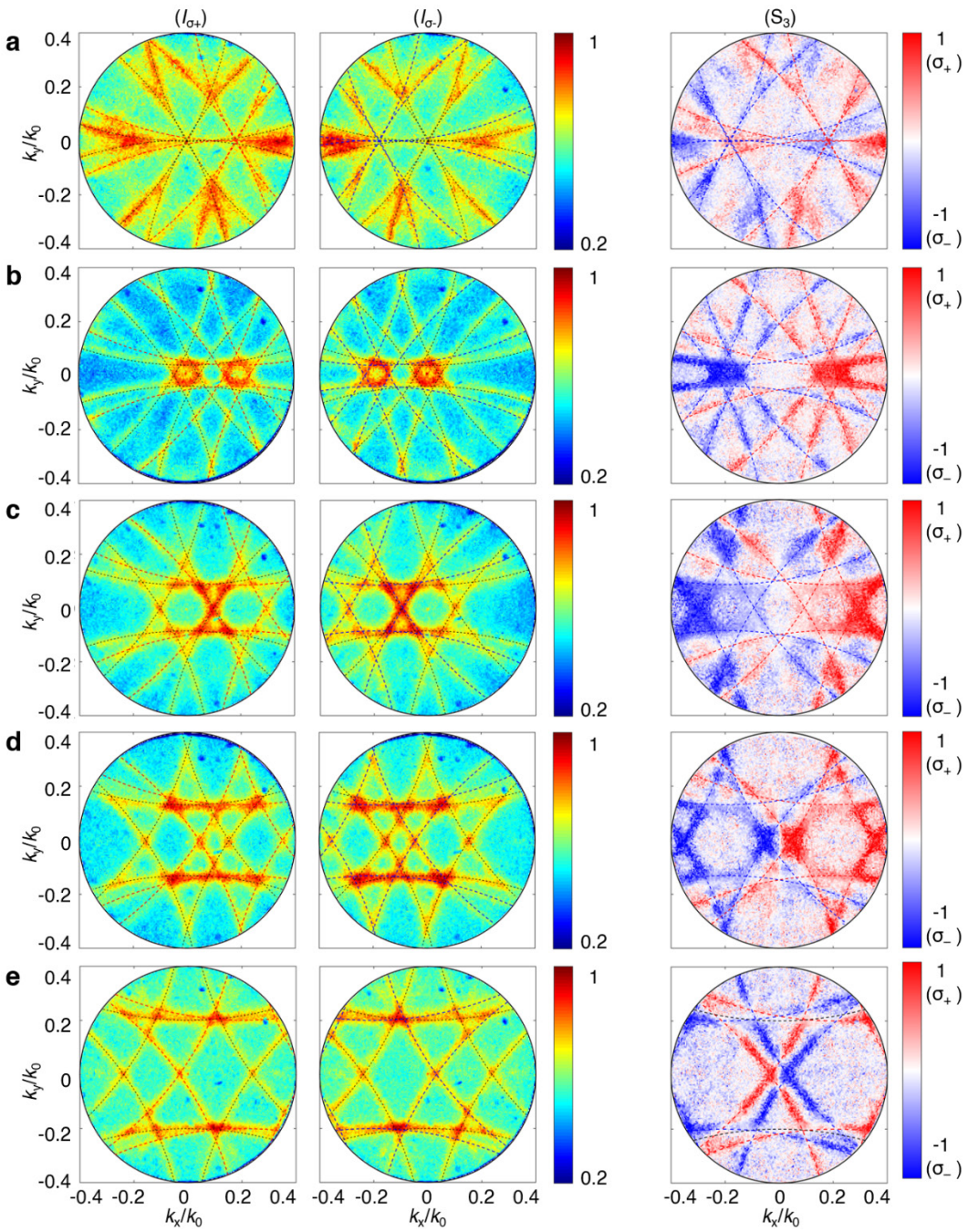

Supplementary Fig. 15 | Measured PL intensity and S_3 distributions in momentum space for Kagome-hexagonal Berry-phase defective PhC incorporated with QDs. a-e correspond to cases with central wavelengths of λ = 700 nm, 720 nm, 740 nm, 760 nm, and 790 nm, respectively. The left and middle columns show the measured PL intensity distributions for the σ_+ and σ_- states, respectively, while the right column shows the corresponding S_3 distributions. The dashed curves denote calculations based on the spin-orbit momentum-matching condition.

Section 11: Chiral modes from conventional GPM without PhC slab

Compared to GPMs utilizing plane waves[4] or surface phonon polariton modes[5] as the light sources (Supplementary Fig. 20), the heterostructures driven by integrated quantum emitters encounter difficulties in achieving geometric phase pickup. Supplementary Fig. 16a depicts the SEM image of a conventional GPM incorporated with QDs, and its measured spin-resolved momentum space is depicted in Supplementary Fig. 16c (see Supplementary Fig. 17 for more results). It is observed that a chiral mode with an inversion-symmetric spin distribution $S_3(-\mathbf{k}_{\parallel}) = S_3(\mathbf{k}_{\parallel})$, rather than an inversion-asymmetric Rashba-type spin split $S_3(-\mathbf{k}_{\parallel}) = -S_3(\mathbf{k}_{\parallel})$, is observed. The same phenomenon is also observed from an array of nanoantennas possessing the same orientation (see SEM image in Supplementary Fig. 16b and results in Supplementary Fig. 22c). These results indicate a negligible geometric phase pickup from anisotropic nanoantennas in the GPM driven by integrated quantum emitters. This is further confirmed by the measured inefficient polarization manipulation of the scattered PL from the nanoantennas (Supplementary Fig. 21c). Instead, the spin split in the chiral mode arises from the chiral near field of the linear dipole emitter[6], which exhibits a four-lobe pattern with alternating helicities (Supplementary Fig. 16d). This spin distribution is remarkable only in the near field and rapidly decays to zero in the far field within $|\mathbf{k}_{\parallel}| \le k_0$. The observable chiral mode is attributed to the discrete near-field sampling by a hexagonal lattice (simplified GPM), which enables the spin accumulations at the radiative modes satisfying the standard momentum-matching condition $\mathbf{k}_{\parallel}^{g,h} = n_{\text{eff}}\mathbf{k}_0 + g\mathbf{G}_1 + h\mathbf{G}_2$, as indicated by the dashed curves in Supplementary Fig. 16c.

The observed chiral mode can be explained via an inefficient interaction between linear dipole emitters and a hexagonal lattice, which scatters the dipole emission without polarization manipulation. We assume a two-dimensional array of dipoles that share the same locations as those of the lattice points at $\mathbf{r}_n$; that is, the dipole $\mathbf{p}_n^{\alpha}$ with random in-plane orientation α is placed above the *n-th* lattice point, where n is an integer labelling the dipoles and lattice points. For a single dipole emitter $\mathbf{p}_m^{\alpha}$, its radiated electric field at the *n-th* lattice point is $\mathbf{E}^{m,\alpha}(\mathbf{r}_n)$. The resultant electric field in momentum space $\mathbf{U}^{m,\alpha}(\mathbf{k}_{\parallel})$ is determined by the coherent addition of the scattered light from all the lattice points

$$\mathbf{U}^{m,\alpha}(\mathbf{k}_{\parallel}) = \mathcal{F}[\sum_{n} \mathbf{E}^{m,\alpha}(\mathbf{r}_n)]. \quad \text{(S1)}$$

Consequently, the corresponding spin distribution in momentum space can be obtained as $S_3^{m,\alpha} = -2\,\mathrm{Im}(U_x^{m,\alpha}U_y^{m,\alpha*}) / (|U_x^{m,\alpha}|^2 + |U_y^{m,\alpha}|^2)$. For multiple independent dipole emitters, the spin-resolved momentum space is determined by the incoherent addition of individual spin distributions, i.e., $\overline{S}_3 = -2\sum_m \mathrm{Im}(U_x^{m,\alpha}U_y^{m,\alpha*}) / \sum_m (|U_x^{m,\alpha}|^2 + |U_y^{m,\alpha}|^2)$. Considering the translational symmetry of the hexagonal lattice, we calculated only a single linear dipole $\mathbf{p}^{\alpha}$ located at one of the lattice points. The calculated $\overline{S}_3(\mathbf{k}_{\parallel})$ for fifty random dipole orientations ($\alpha \in (0, 2\pi]$) is shown in Supplementary Fig. 16e, in agreement with the measurement (Supplementary Fig. 16c).

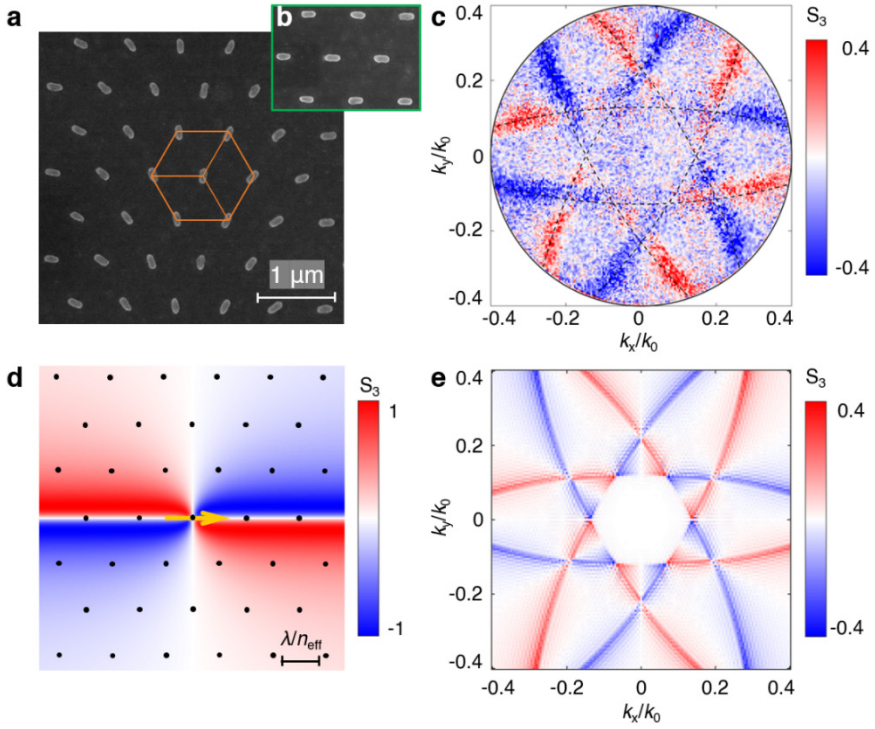

Supplementary Fig. 16 | Chiral modes from conventional GPM incorporated with QDs a, SEM image of a hexagonal GPM. Its structural parameters are the same as those in Fig. 4c, except for the absence of the Kagome PhC slab. **b**, Similar to **a** with all the nanoantennas in the same orientation $\theta(x,y) = 0$. **c**, Measured chiral mode in momentum space at λ = 760 nm. The dashed black curves denote calculations based on the standard momentum-matching condition. **d**, Calculated S_3 distribution of the near field for an x-oriented dipole. The hexagonal lattice (black dots) indicates the simplified GPM. **e**, Calculated chiral mode in momentum space for a linear dipole emitter with fifty random orientations.

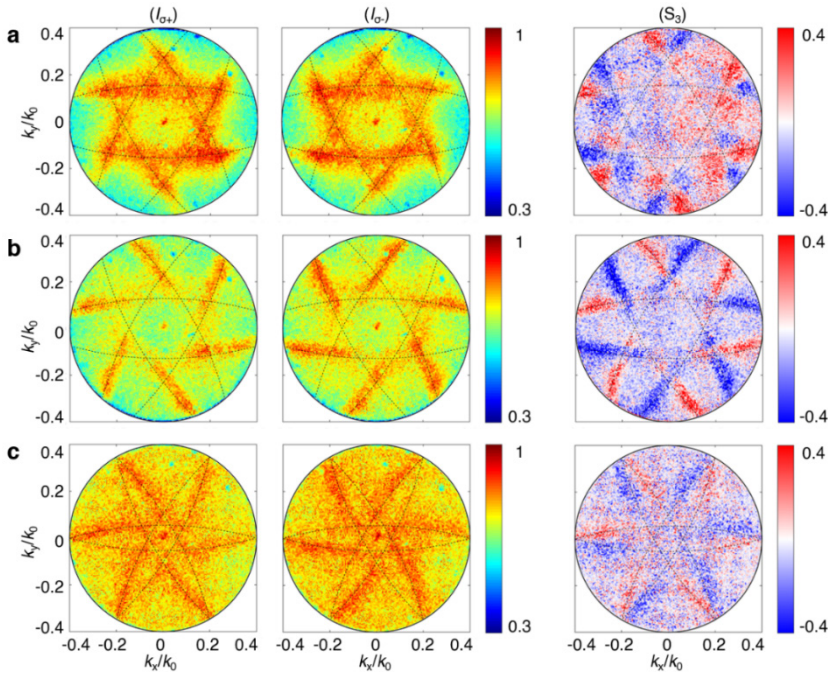

Supplementary Fig. 17 | Measured PL intensity and S_3 distributions in momentum space for conventional GPM incorporated with QDs. a-c correspond to cases with central wavelengths of λ = 740 nm, 760 nm, and 790 nm, respectively. The left and middle columns show the measured PL intensity distributions for the σ_+ and σ_- states, respectively, while the right column shows the corresponding S_3 distributions. The dashed black curves denote calculations based on the standard momentum-matching condition.

Alternatively, due to the C_6 rotational symmetry of the hexagonal lattice, the random-oriented dipole possesses six primary orientations, which can be further reduced to three ($\mathbf{p}^{\alpha}$, α = 0, π/3, 2π/3) because two dipoles with opposite orientations give the same spin distribution. The dipole emitter with each orientation produces a mirror-image asymmetric spin distribution in momentum space, where the mirror axis is perpendicular to (or along) the dipole orientation. Moreover, the incoherent addition of the three spin distributions gives rise to a net chiral distribution (Supplementary Fig. 18), which also matches with our measurement (Supplementary Fig. 16c).

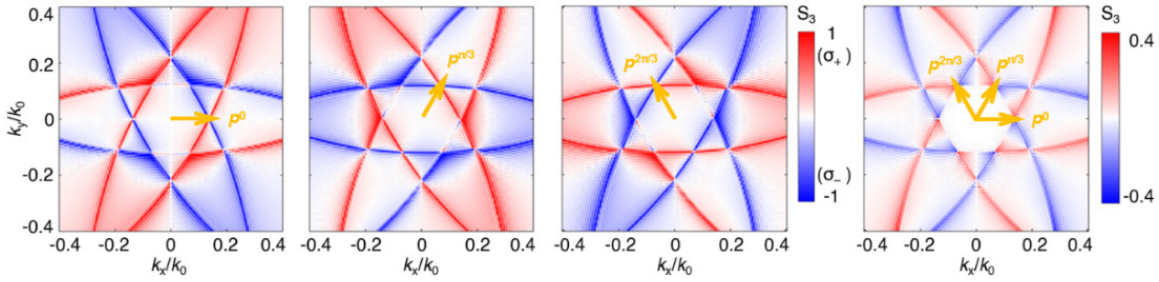

Supplementary Fig. 18 | Calculated chiral modes in momentum space for linear dipole emitter along primary orientations and their incoherent addition. The dipole orientations are indicated by the orange arrows.

Evolution from chiral mode to photonic Rashba effect

As demonstrated earlier, the chiral mode and the photonic Rashba effect originate from a weak and a strong polarization manipulation of the linear dipole emission by the nanoantennas, respectively. Here, we demonstrate the evolution from the chiral mode to the photonic Rashba effect by controlling the extinction ratio of the nanoantenna. For convenience, the nanoantennas in the GPM are described by an equivalent method of Jones calculus in terms of polarization manipulation. The *n-th* anisotropic nanoantenna with orientation θ_n can be considered as a partial polarizer described by the Jones matrix

$$T_n = \begin{bmatrix} 1\text{-}\xi\sin^2\theta_n & \xi\cos\theta_n\sin\theta_n \\ \xi\cos\theta_n\sin\theta_n & 1\text{-}\xi\cos^2\theta_n \end{bmatrix}. \tag{S2}$$

Herein, ξ is the parameter describing the extinction ratio of the nanoantenna. Specifically, $\xi = 0$ indicates no polarization manipulation from the nanoantenna, while $\xi = 1$ indicates complete polarization manipulation along the nanoantenna's orientation θ_n. For a single dipole emitter $\mathbf{p}_m$, its radiated in-plane electric field components at the *n-th* nanoantenna are $E_x^m(\mathbf{r}_n)$ and $E_y^m(\mathbf{r}_n)$. The resultant in-plane electric field components $U_x^m(\mathbf{k}_\parallel)$ and $U_y^m(\mathbf{k}_\parallel)$ in momentum space are determined by the coherent addition of the scattered light from all the nanoantennas:

$$\begin{bmatrix} U_x^m(\mathbf{k}_\parallel) \\ U_y^m(\mathbf{k}_\parallel) \end{bmatrix} = \mathcal{F}\{\sum_n T_n \begin{bmatrix} E_x^m(\mathbf{r}_n) \\ E_y^m(\mathbf{r}_n) \end{bmatrix}\}. \tag{S3}$$

Supplementary Fig. 19 depicts the calculated spin-resolved momentum spaces $\overline{S}_3(\mathbf{k}_\parallel)$ for different values of ξ. It is observed that, for $\xi = 0$ and $\xi = 1$, only the chiral mode and the photonic Rashba effect are observed, respectively. As for $\xi \in (0,1)$, both the chiral mode and the photonic Rashba effect can be observed, and the ratio between them is determined by $(1-\xi)/\xi$. Hence, there is no transition between these two phenomena, and we intentionally use "evolution" to describe this process. Moreover, the photonic Rashba effect is not a subset of the chiral mode due to their distinct physical mechanisms: the former is due to the Berry phase defect mode generated by the space-variant polarization manipulation, while the latter is originated from the chiral near field of the linear dipole emitter.

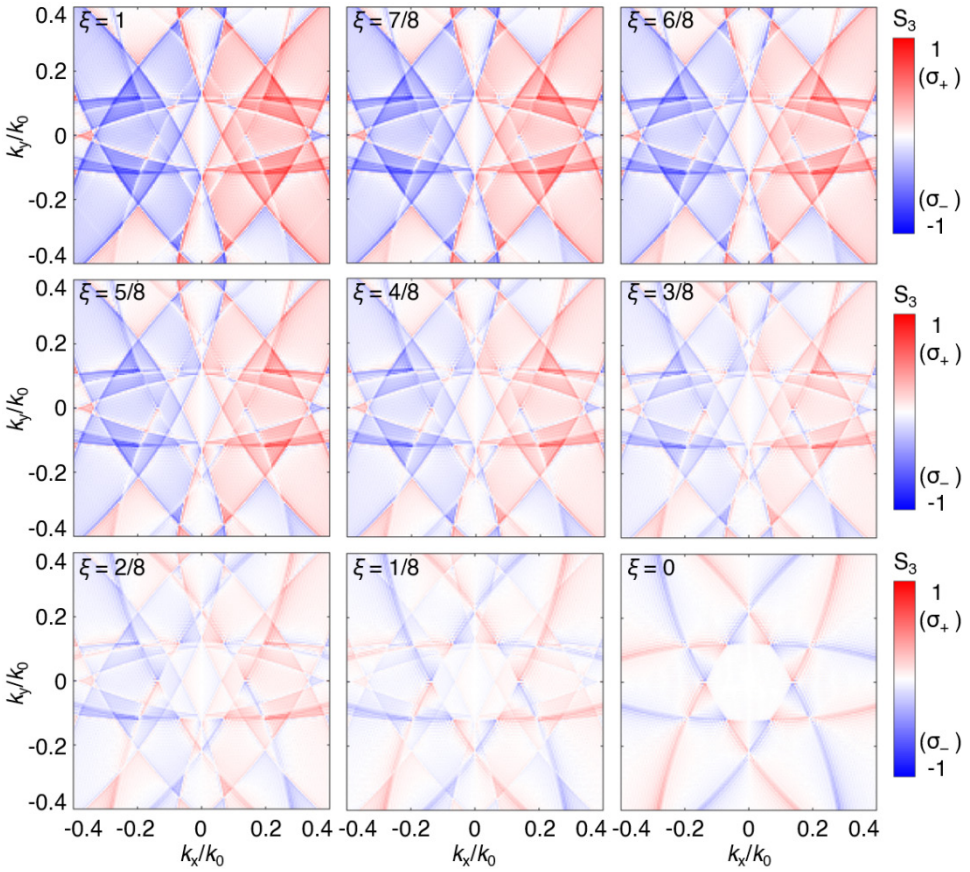

Supplementary Fig. 19 | Evolution from chiral mode to photonic Rashba effect. For each value of ξ, twelve linear dipole emitters, located at the nanoantenna locations in one unit cell of the GPM, are considered.

Measurement for plane-wave illumination

For comparison, the Kagome-hexagonal Berry-phase defective PhC (Fig. 4c) and hexagonal GPM (Supplementary Fig. 16a) were also characterized by on-axis plane waves (λ = 760 nm), and their spin-resolved intensity distributions in momentum space are displayed in Supplementary Fig. 20. For both structures, we can observe two spots with opposite spin states in the ±1 diffraction order (indicated by orange arrows). These spin-split spots stem from an additional momentum acquired from the gradient of geometric phase pickup; that is, $\mathbf{k}_{\mathrm{a}} = \nabla\phi_{\mathrm{g}}(x,y) = [-2\sigma\partial\theta(x,y)/\partial x]\hat{\mathbf{x}}$. Nevertheless, the GPM shows a negligible geometric phase pickup when interacting with the incorporated QDs, due to the weak polarization manipulation of the scattered PL by the nanoantennas (Supplementary Fig. 21c). In contrast, the geometric phase-induced Rashba-type spin split is observed from the Berry-phase defective PhC (Fig. 4e), wherein the Berry phase defect mode enables a strong polarization manipulation of the scattered PL (Supplementary Fig. 21a).

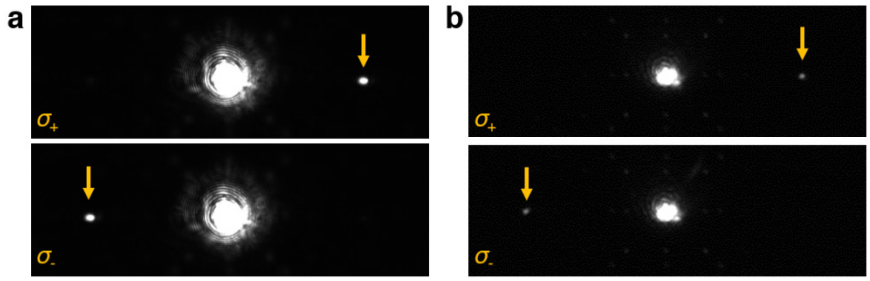

Supplementary Fig. 20 | Measured spin-split spots in momentum space under plane-wave illumination. a, Hexagonal GPM. **b**, Kagome-hexagonal Berry-phase defective PhC. The orange arrows indicate the ±1 diffraction order.

Measurement for reference structures

To experimentally verify that the Berry-phase defective PhC enables a strong polarization manipulation, we also fabricated reference structures incorporated with QDs (Supplementary Fig. 21). The schematic in Supplementary Fig. 21a shows a defective PhC with an array of anisotropic defects possessing the same orientation. Due to the polarization locking from the coupled defect mode, the scattered PL is strongly polarized along the orientation of the defects, that is, *x* polarization, as shown by the measurements in Supplementary Fig. 21a. The measured *x*- and *y*-polarized PL intensity distributions agree with the calculated $|U_x|^2$ and $|U_y|^2$ distributions, respectively, by assuming *x*-polarized dipole emitters in equation (1). This phenomenon demonstrates the strong polarization manipulation from anisotropic defects embedded within the PhC slab, which plays an essential role in the observed photonic Rashba effect. In contrast, the strong polarization manipulation disappears when the anisotropic defects are replaced with isotropic ones or the PhC slab is removed (Supplementary Figs. 21b and c). The measured *x*- and *y*-polarized PL intensity distributions also agree with the calculated $|U_x|^2$ and $|U_y|^2$ distributions, respectively, by assuming both *x*- and *y*-polarized dipole emitters in equation (S1).

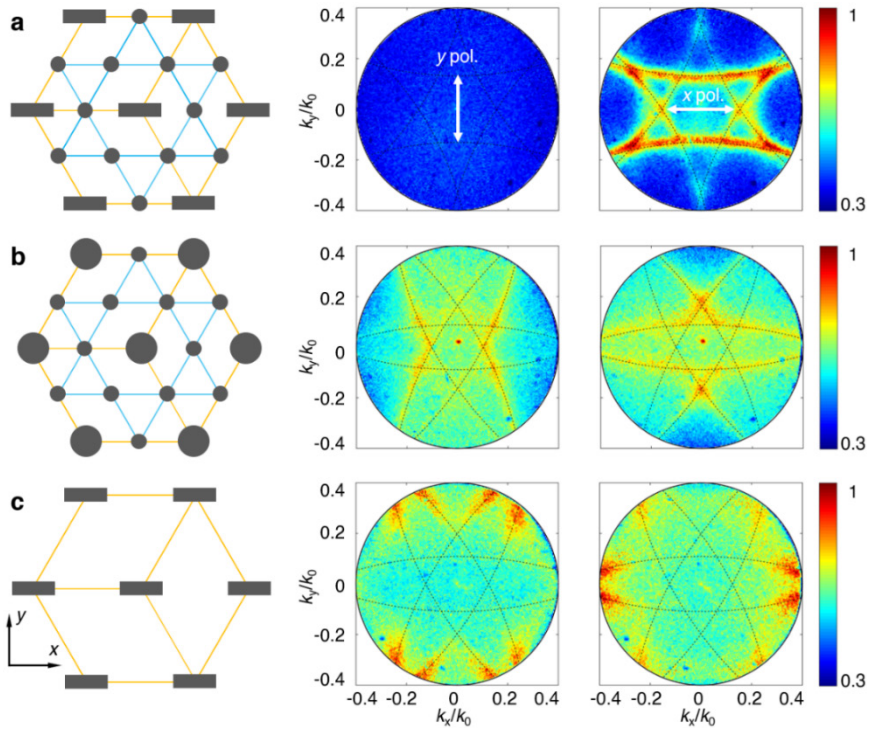

Supplementary Fig. 21 | Measured PL intensity distributions in momentum space under orthogonal linear polarization states. a, Defective PhC with an array of anisotropic defects possessing the same orientation $\theta(x,y) = 0$. **b**, Defective PhC with an array of isotropic defects. **c**, Similar to **a** without the PhC slab. The left column shows the schematics of the reference structures; the middle and right columns show the *y*- and *x*-polarized PL intensity distributions in momentum space, respectively. The central wavelengths for the three cases are 760 nm. The dashed black curves denote calculations based on the standard momentum-matching condition.

Due to the distinct polarization manipulation abilities of the three configurations, different spin-enabled phenomena are observed in momentum space (Supplementary Fig. 22). Although the anisotropic defects embedded within the PhC slab enable a strong polarization manipulation of the scattered PL along the *x* direction, no spin-split phenomenon is observed due to the absence of space-variant variations (Supplementary Fig. 22a). The chiral modes are observed for the other two cases: the defective PhC with isotropic defects and the isolated nanoantenna array (Supplementary Figs. 22b and c). These chiral modes can also be explained via an inefficient interaction between the chiral near field of linear dipole emitter and a hexagonal lattice. Note that, due to a weak anisotropic excitation of the *x*- and *y*-polarized linear dipoles ($p_x : p_y = 1 : 0.75$), the chiral mode in Supplementary Fig. 22c is slightly different from the expected one, such as that in Supplementary Fig. 16e.

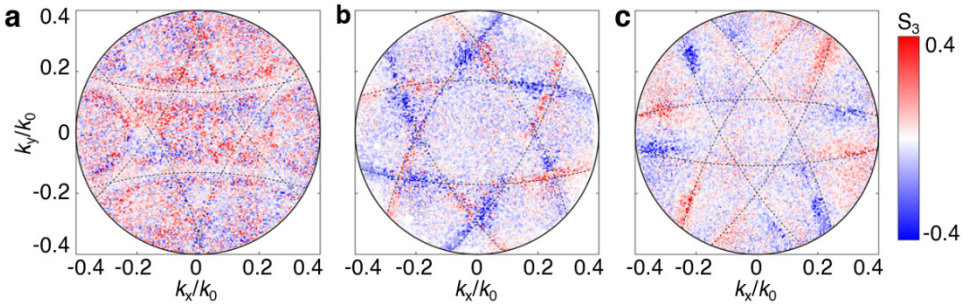

Supplementary Fig. 22 | Measured S_3 distributions in momentum space. a-c correspond to the three configurations shown in Supplementary Figs. 21a-c, respectively. The central wavelengths for the three cases are 760 nm, 720 nm, and 760 nm, respectively. The dashed black curves denote calculations based on the standard momentum-matching condition.

References

1. Sortino, L. *et al.* Enhanced light-matter interaction in an atomically thin semiconductor coupled with dielectric nano-antennas. *Nat. Commun.* **10**, 5119 (2019).
2. Xu, Y., Lee, R. K. & Yariv, A. Quantum analysis and the classical analysis of spontaneous emission in a microcavity. *Phys. Rev. A* **61**, 033807 (2000).
3. Bomzon, Z., Biener, G., Kleiner, V. & Hasman, E. Space-variant Pancharatnam-Berry phase optical elements with computer-generated subwavelength gratings. *Opt. Lett.* **27**, 1141-1143 (2002).
4. Lin, D., Fan, P., Hasman, E. & Brongersma, M. L. Dielectric gradient metasurface optical elements. *Science* **345**, 298-302 (2014).
5. Dahan, N., Gorodetski, Y., Frischwasser, K., Kleiner, V. & Hasman, E. Geometric Doppler effect: spin-split dispersion of thermal radiation. *Phys. Rev. Lett.* **105**, 136402 (2010).
6. Neugebauer, M., Banzer, P. & Nechayev, S. Emission of circularly polarized light by a linear dipole. *Sci. Adv.* **5**, eaav7588 (2019).